Tectonophysics 862 (2023) 229987

Contents lists available at ScienceDirect

Tectonophysics

journal homepage: www.elsevier.com/locate/tecto

Laboratory simulation of fault reactivation by fluid injection and implications for induced seismicity at the BedrettoLab, Swiss Alps

G. Volpe [a,*], G. Pozzi [b], C. Collettini [a,b], E. Spagnuolo [b], P. Achtziger-Zupančič [c], A. Zappone [d], L. Aldega [a], M.A. Meier [d], D. Giardini [d], M. Cocco [b]

[a] Department of Earth Sciences, La Sapienza University of Rome, Italy
[b] Istituto Nazionale di Geofisica e Vulcanologia, Italy
[c] Department of Engineering Geology and Hydrogeology, RWTH Aachen University, Germany
[d] Department of Earth Sciences, ETH, Zürich, Switzerland

A B S T R A C T

Fluid induced fault reactivation experiments will take place as part of the "Fault Activation and Earthquake Rupture" project (FEAR) at the BedrettoLab, an underground laboratory for geosciences and geo-energy excavated within the Rotondo massif (Swiss Alps). The aim of this publication is to characterize frictional properties and permeability of the main segment of the fault zone selected for limited fluid-induced fault reactivation experiments. Firstly, we characterized fault zone microstructures in the field and in thin sections. Secondly, we assessed fault gouge mineralogy by X-ray powder diffraction analysis, yielding a composition in agreement with similar fault gouges in the same area. Finally, we performed a detailed frictional and permeability characterization in laboratory, using BRAVA (Brittle Rock deformAtion Versatile Apparatus). We performed five frictional experiments, run at the actual in-situ conditions: four experiments for frictional properties characterization; and one further experiment where we stimulated the experimental fault by fluid pressurization applying a similar injection protocol designed for the in-situ hydraulic stimulation experiment. Additionally, we performed microstructural analysis on experimental samples to link frictional and permeability properties with fault fabric evolution. The integration of experimental results with field investigations suggests that the selected fault is potentially seismogenic and can be dynamically reactivated and controlled with hydraulic stimulation. This study highlights the importance of bridging the gap between laboratory and in-situ fault characterization, where experimental results become instrumental for the correct design of injection protocols such as those of FEAR project.

1. Introduction

1.1. The BedrettoLab and the FEAR project

The Bedretto Tunnel is a 5218 m long tunnel located in the Swiss Central Alps (Fig. 1). It links the Bedretto Valley with the Furka Base Tunnel, passing through the Rotondo massif (Keller and Schneider, 1982). The orientation of the tunnel is approximately N 317°. The rock overburden has a maximum height of 1632 m below the Pizzo Rotondo peak (3124 m a.s.l., Fig. 1b). Access to the tunnel was granted in 2018 to the ETH Zürich by the owner, the Matterhorn Gotthard Bahn, for long-term research programs, leading to the establishment of the world unique Bedretto Underground Laboratory for Geosciences and Geo-energy (BULGG or the BedrettoLab, Fig. 1b).

Since its completion, the tunnel remained largely unpaved and unlined, thus offering the unique opportunity to characterize in-situ the geological properties (structural and hydrological among others) of the host rock. Detailed investigations were previously carried out along the tunnel, including studies on the groundwater systems (Lützenkirchen, 2002; Ofterdinger, 2001), the brittle fault zones structures (Lützenkirchen, 2002; Lützenkirchen and Loew, 2011), and the ductile shear zones and associated geochronology (Rast, 2020; Rast et al., 2022; Ceccato et al., 2023).

This tunnel, extensively instrumented thanks to the BedrettoLab, provides an exceptional facility and a fully monitored area that can be exploited for observing earthquake processes at closer distance. In the Bedretto underground experimental site it is possible to perform experiments of induced seismicity by fluid-induced stimulation of natural faults with an unprecedented level of in-situ instrumentation compared to previous similar project (e.g., the JAGUARS project, Nakatani et al., 2008, or the NELSAM project, Reches, 2006). For this purpose, the European Research Council (ERC) funded the "Fault Activation and Earthquake Rupture" (FEAR) Synergy project that grouped scientists from the Eidgenössiche Technische Hochschule Zürich (ETH Zurich) in Switzerland, the Rheinisch-Westfälische Hochschule (RWTH Aachen University) in Germany, and the Instituto Nazionale di Geofisica e

* Corresponding author.
E-mail address: giuseppe.volpe@uniroma1.it (G. Volpe).

https://doi.org/10.1016/j.tecto.2023.229987
Received 20 March 2023; Received in revised form 30 June 2023; Accepted 6 July 2023
Available online 11 July 2023

Vulcanologia (INGV) in Italy. The main goal of the FEAR project is to perform limited and controlled fault stimulation experiments at 50-100 m scale and over 1 km of depth with real-time control of experimental conditions and monitoring.

Thanks to the wide range of expertise of scientists involved in the project, FEAR is aiming to provide a full in-situ characterization of all seismological, geological, and engineering features, concerning fault instability due to hydraulic stimulation. The careful selection of candidate fault for injection and reactivation has been thus one of the fundamental aspects of the first part of the project. The selected fault is set at 2378 m from the tunnel entrance, corresponding in the tunnel structures database to the fault n. 48.5 (yellow star in Fig. 1 and Fig. SI.1 in Supporting Information). The name "MC fault", assigned by the FEAR team, will be used throughout the text to refer to the selected fault. The aim of this study is to characterize: the frictional and hydraulic properties of the MC fault as well as its natural and experimental microstructures in the laboratory. We hereby report: the description of the main segment (the portion where most deformation has been accommodated) of the MC fault zone from the outcrop scale to the thin section; the X-ray diffraction analysis of the fault gouge; the mechanical, frictional, and permeability properties of the same material measured with laboratory experiments. We also show the results of fluid injection tests performed in the laboratory, using in-situ boundary condition and a similar injection protocol envisioned for the main FEAR experiments.

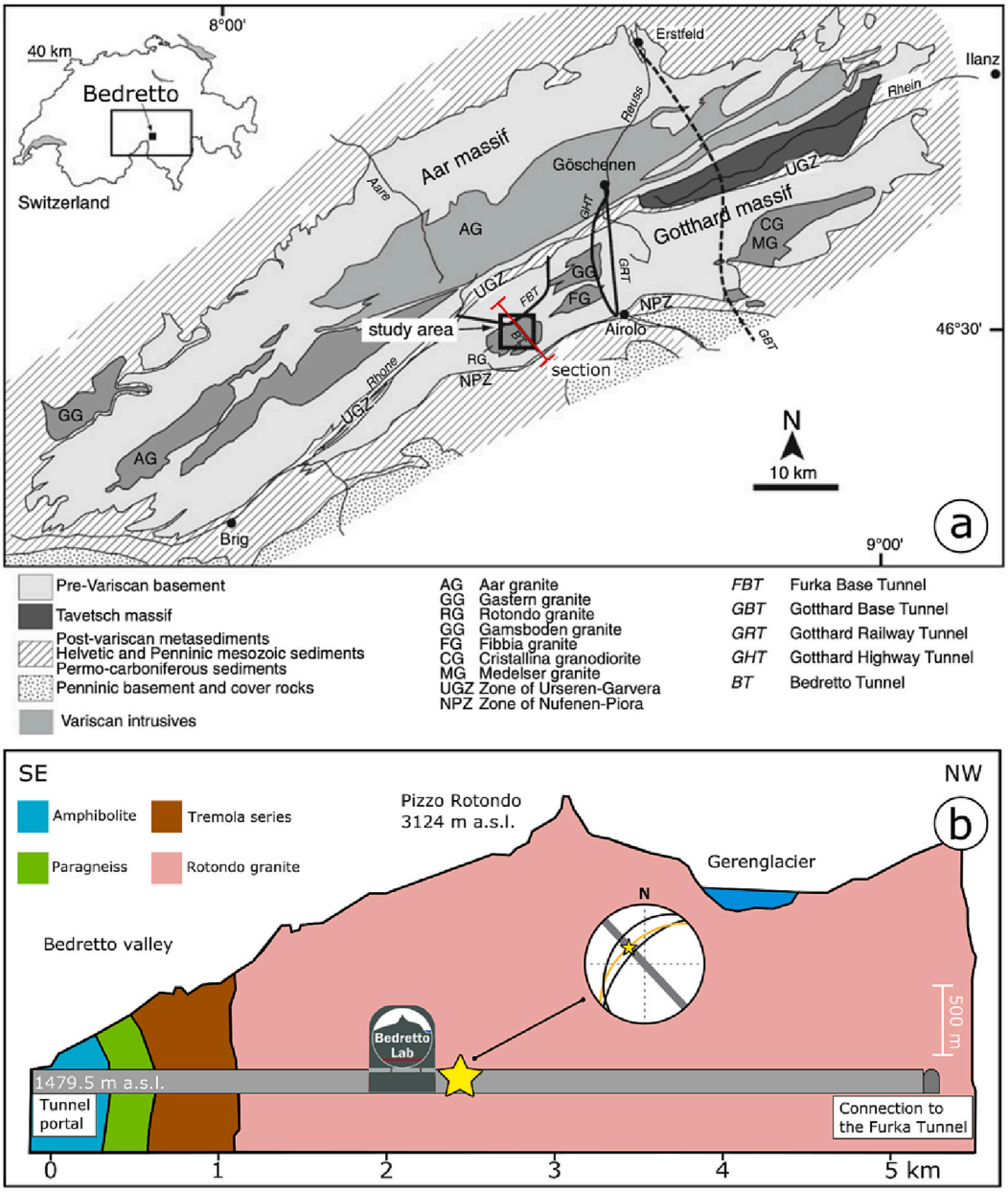

Fig. 1. Geographical and geological setting of the study area. a) Geological map of the Gotthard and Aar Massif (Central Swiss Alps) with study area and trace (red line) of the geological cross section in panel b (modified after Lützenkirchen and Loew, 2011). b) Cross section of the Bedretto tunnel, indicating all the geological units intersected by the tunnel. Yellow star indicates the intersection of the MC fault (dip and dip direction: 58°/318°) with the tunnel (direction: 317° N). Image modified after Ma et al., 2022. The stereoplot includes the three main segments of the MC fault with highlighted in yellow the selected segment and in gray the tunnel direction. (For interpretation of the references to colour in this figure legend, the reader is referred to the web version of this article.)

2. Fault characterization

2.1. Geological setting

The Bedretto Tunnel is entirely hosted within the Helvetic domain of the western Alps (Fig. 1). The tunnel crosses different rocks series which are, in order from the entrance, the Tremola series, the Prato series, and the Rotondo granite (Lützenkirchen, 2002; Lützenkirchen and Loew, 2011; Ma et al., 2022; Rast et al., 2022). The BedrettoLab is mainly located within the Rotondo granite (Fig. 1b), with a local overburden of ~1000 m. The Rotondo intrusion is one of various plutons within the Gotthard massif (Gamsboden, Rotondo, Medelser, Cristallina, and Fibbia) emplaced at 294 ± 1.1 Ma (Sergeev et al., 1995) during the Variscan orogeny. Successively the Rotondo granite experienced various metamorphic and tectonic phases related to the late Variscan and Alpine orogeny, recorded by several sets of ductile and brittle shear zones. Ductile deformation within the Rotondo granite is localized in a few, foliated mylonitic shear zones (Schneider, 1985; Lützenkirchen and Loew, 2011; Rast et al., 2022; Ceccato et al., 2023). Brittle structures (e.g., fractures and brittle faults) are less common and often exploit pre-existing discontinuities such as ductile shear zones (Lützenkirchen, 2002; Lützenkirchen and Loew, 2011; Ceccato et al., 2023). In the Aar Massif area, brittle deformation is responsible for moderate seismicity ($M < 2$) that occurs on faults trending ~110° N with both extensional and strike-slip kinematics (Kastrup et al., 2004; Diehl et al., 2018; Heidbach et al., 2018; Ma et al., 2022). Stress analysis suggests that transition from normal to strike slip faulting is expected with increasing depth (Ma et al., 2022).

Several medium-to-large scale ductile and minor brittle shear zones are visible along the tunnel walls. These structures are concordant (in terms of orientation) with those observed by scanline mapping and remote sensing of the surface above the tunnel (Jordan, 2019; Ceccato et al., 2023). A complete mapping and in-detail studies of these structures are reported in literature (Lützenkirchen, 2002; Lützenkirchen and Loew, 2011; Jordan, 2019; Rast et al., 2022; Ceccato et al., 2023). The most frequent shear zones belong to an *E*-W striking, steeply dipping set, which are roughly oriented perpendicularly to the tunnel. Tunnel-parallel shear zones are significantly under-sampled (Rast et al., 2022). Generally, all the shear zones dip at high angle (>50°) toward south or north. The host rock is a metagranite from greenschist to amphibolite facies, containing quartz, plagioclase, K-feldspar, and muscovite. Biotite, chlorite, and garnet occur as minor phases (~30% quartz, ~55% feldspars, ~10% phyllosilicates, ~5% accessory, Hafner, 1958; Labhart, 2005; Rast et al., 2022).

Ductile shear zones occur along lithological contacts, such as the boundaries of mafic enclaves (Rast et al., 2022) or lamprophyre dykes, and are characterized by a reverse to strike-slip kinematics (Lützenkirchen, 2002; Rast et al., 2022). Shear zones are foliated with biotite and elongated quartz ribbons (Rast et al., 2022). The age of the ductile deformation is still a matter of debate. According to some authors ductile deformation is related to the late Variscan orogenic phase (Lützenkirchen, 2002; Lützenkirchen and Loew, 2011), for others is driven by the Alpine orogeny (Labhart, 2005). Brittle faults are preferentially localized along the pre-existing ductile shear zones, in particular the ones that are perpendicular to the tunnel and dip toward north (Lützenkirchen, 2002 and Lützenkirchen and Loew, 2011). Brittle faults generally have normal or strike-slip kinematics (Lützenkirchen and Loew, 2011; Jordan, 2019; Rast et al., 2022) and often have fault cores containing a whitish gouge. According to some authors, these faults can be potentially active with extensional kinematics in the framework of the actual stress field, which favors normal faulting in the high-altitude parts of the Alps (Heidbach et al., 2018; Kastrup et al., 2004; Diehl et al., 2018). The water inflow (up to 0.6 l/s) in the tunnel is primarily associated to diffused fracturing and localized faults (Lützenkirchen, 2002; Ofterdinger, 2001; Arnet, 2021). The tunnel-perpendicular faults with gouges are the most conductive structures and have high water inflows (Ma et al., 2022; Rast et al., 2022).

2.2. MC fault structure and mineralogy

A detailed characterization of the entire MC fault zone has been presented by Ceccato (Ceccato et al., 2023) and Achtziger-Zupančič in the FEAR Geology Working-Group report (written communication). In this work we focus on one of the main segments of the MC fault. The MC fault belongs to the category of the brittle faults that contain a core of fine-grained cataclasites (e.g., Lützenkirchen and Loew, 2011). The dip direction is between 315° and 335° N with a plunge of 50° to 70° and exploits a narrow mylonitic shear zone characterized by biotite decorated quartz veins parallel to the foliation. Macroscopically, the brittle deformation is localized at the splitting between the quartz vein and the mylonitic wall rock. The MC fault appears as a very localized shear zone composed of a principal narrow fault core (average thickness < 5 mm) filled by a whitish fault gouge (Fig. 2a, b) and by coarser cataclasites, which are only observed locally at dilational jogs. The fault itself does not show a well-developed damage zone, but rather the damage is a characteristic of the host rock showing a network of neat fractures. The deformation that produced the gouge at the core of the MC fault seems to overprint all the previous phases of ductile and cataclastic deformation occurred at higher temperatures than the last (strike-slip) occurred in zeolite facies, Lützenkirchen and Loew, 2011; Ceccato et al., 2023), suggesting repeated fault reactivations even in the current regional stress field (Kastrup et al., 2004; Lützenkirchen and Loew, 2011; Heidbach et al., 2018). The absence of clear kinematic indicators in the gouge does not allow to retrieve the shear-sense of faulting. However, it is possible to observe a relative displacement of ~10 cm at a dilational jog (yellow triangles in Fig. 2a), which suggest an extensional kinematics component.

The fault core was carefully sampled for microstructural investigation together with the host rock (Fig. 2b) and mounted to produce a petrographic thin section (30 μm thick, Fig. 2c). Four distinct zones can be separated by microstructural analysis (see Fig. SI.2). The first is the host rock, a protomylonitic granite composed by coarse (~1 cm) grains of K-feldspar, quartz and albite, and a finer fraction of the same minerals organized in anastomosing, discontinuous seams. Coarse grains of quartz and feldspars show undulose extinction and polygonization (subgrains). Evidence of bulging is found locally along the grain boundaries. The second zone is composed of more continuous, anastomosing ultramylonitic shear zones, which present homogenous grain size (< 100 μm, Fig. 2c), quadruple junctions, and a shear-parallel C-foliation, defined by oriented grains of biotite (Fig. 2c and Fig. SI.2 in Supporting Information). The brittle fault core (third zone) is formed by a thin layer of sub-rounded quartz and feldspar clasts (< 50 μm) embedded in a matrix of white mica and finer granular materials, defining a weak C-foliation. The last zone is a zeolite-rich vein localized at one side of the fault core, characterized by a crosshatch pattern of crystals (up to few mm in length) that suggests static growth. Some isolated zeolites lumps are also found in the cataclastic layer (e.g., Lützenkirchen and Loew, 2011). Like the MC fault, they are described as localized cataclastic shear zones that overprint previous mylonitic foliation (Lützenkirchen and Loew, 2011; Ceccato et al., 2023).

The fault gouge is incohesive (Fig. 2a). The gouge sample was oven dried at 45 °C for 48 h. Agglomerates were then gently dismembered by hand to avoid contamination of the original grain size and coarse clasts were removed by hand. Most of the gouge in the thin principal slip zone is fine-grained (< 125 μm) as revealed by thin section analysis (Fig. 2d). We therefore sieved the material below 125 μm to minimize the contamination of the coarser, outer cataclasite, which is unavoidably collected with the sampling procedure in situ.

Mineral assemblage of the sieved gouge has been assessed by X-Ray powder Diffraction (XRpD) analysis. We used a Bruker D8 Advance X-ray system provided with Lynxeye XE-T silicon-strip detector. The analysis was performed using CuKα radiation (λ = 1.5406 Å) at 30 mA

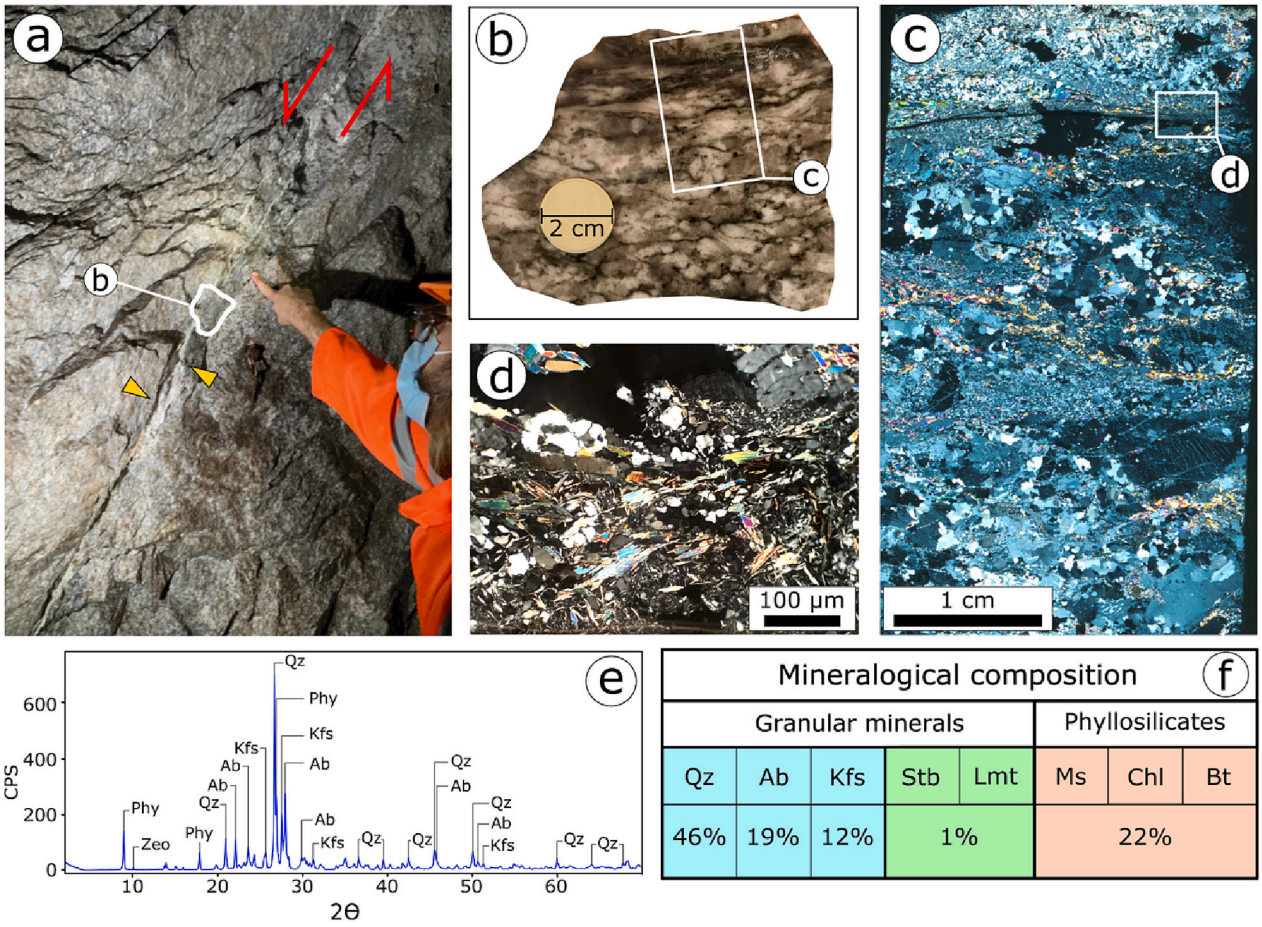

Fig. 2. Structural and mineralogical characterization of the MC fault. a) Outcrop view of the selected fault in the tunnel, yellow triangles indicate conjugate point across an extensional jog; b) hand specimen of the fault zone recovered from the fault (white inset in panel a); c) crossed polars view of the fault zone in thin section (white box in panel b). d) closeup of the principal shear zone from the white box in panel c; e) XRpD pattern of the gouge from the principal shear zone (panel d); f) mineralogical assemblage of the gouge from the selected fault. Phy: phyllosilicates; Zeo: zeolites; Qz: quartz; Ab: albite; Kfs: K-feldspars; Stb: stilbite; Lmt: laumontite; Ms.: muscovite; Chl: chlorite; Bt: biotite. (For interpretation of the references to colour in this figure legend, the reader is referred to the web version of this article.)

and 40 kV. Powders were analyzed between 2 and 70° 2θ with steps of 0.02° 2θ while spinning (e.g., Volpe et al., 2022a). The semiquantitative assessment of mineral assemblage was obtained by the calculation of the peak areas and by using as calibration constants the mineral intensity factors (Moore and Reynolds Jr., 1997). The XRpD analysis of the gouge (Fig. 2e) yields a mineral assemblage dominated by granular silicates (quartz, albite, and K-feldspar) that constitute the 77% of the whole rock composition and by phyllosilicates, mostly muscovite and minor chlorite and biotite (22% in total). Zeolite minerals such as stilbite and laumontite occur as minor phases with content of 1% (Fig. 2f). The observed bulk mineralogical composition is consistent with analyses performed on other brittle faults, dissecting the Rotondo granite (see Lützenkirchen and Loew, 2011).

3. Frictional experiments

We performed frictional experiments to explore the frictional properties of the material composing the MC fault core. The sieved powders were tested with BRAVA, a biaxial apparatus (Collettini et al., 2014) at the INGV in Rome. We employed double direct shear configuration (DDS) consisting of three grooved steel forcing blocks squeezing two equal gouge layers (Fig. 3c, and details in paragraphs 3.1.1 and 3.1.2). Normal stress (σ_n) is exerted perpendicular to the sample layers by a horizontal fast-acting servo-controlled hydraulic piston. A second piston (vertical) exerts shear stress (τ) on the central block and promotes shear deformation within the two gouge layers. The load exerted by the pistons is measured via strain-gauged load-cells installed at the piston end, with an accuracy of ±0.03 kN in a range between 0.2 kN and 1.5 MN (Collettini et al., 2014). The load is converted to stress by dividing it by the area of contact of the forcing blocks (50 by 50 mm). Displacement is measured by linear variable displacement transformers (LVDTs) with an accuracy of ±0.01 µm. Load point displacement of horizontal and vertical pistons was corrected for the elastic deformation of the experimental apparatus, knowing that the apparatus stiffnesses are 928.5 kN/mm on the vertical axis and 1283 kN/mm on the horizontal axis (Collettini et al., 2014; Giorgetti et al., 2015). The elastic response of the entire apparatus is linear at the selected experimental conditions. One experiment is carried out within the machine vessel using a jacketed DDS and applying pressure with vaseline-based oil as confining medium. This assembly is instrumented to allow control of fluid circulation perpendicular to the gouge layers across the entire area of the lateral blocks. The confining pressure (P_c), the upstream (P_u) and downstream (P_d) fluid pressures are exerted by three hydraulic servo-controlled intensifiers. Intensifier displacements are measured by LVDTs, accurate to ±0.1 µm, and fluid pressures by transducers, with an accuracy of ±7 kPa (Collettini et al., 2014). We used $CaCO_3$-equilibrated water, similar to those circulating in the massif, to saturate the samples.

3.1. Experimental methods and procedures

3.1.1. Frictional tests

The MC fault gouge was tested with two types of experiments. The

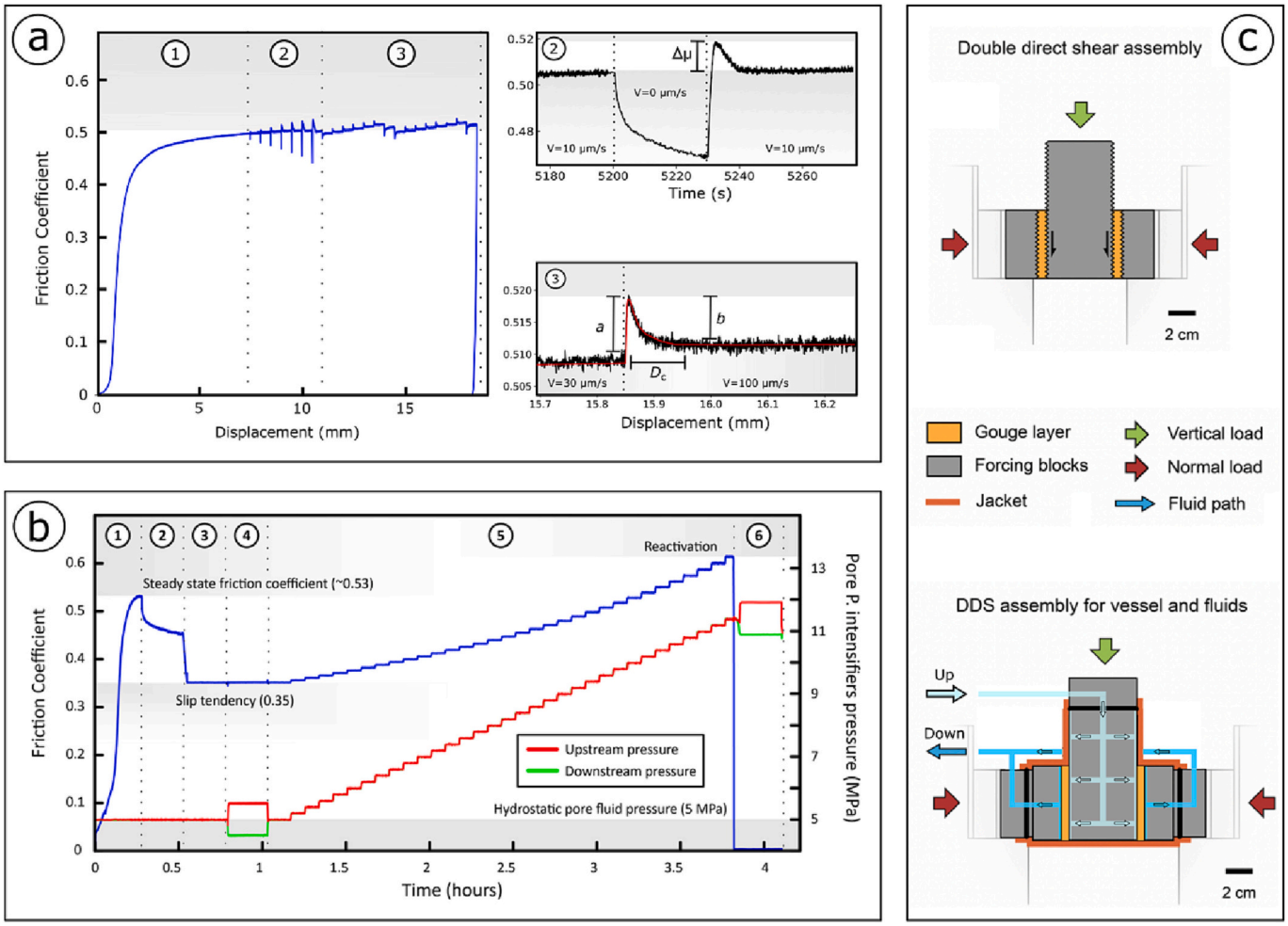

Fig. 3. Experimental procedures, frictional analysis, and experimental assemblage. a) experimental design and procedures for the standard characterization of the RSF parameters. Stage 1: run-in where frictional strength is measured. Stage 2: slide-hold-slide test where frictional restrengthening is measured. Stage 3: velocity step tests where the velocity dependence of friction is evaluated b) experimental design of the injection experiment. Stage 1: run-in. Stage 2: hold phase and decelerating creep. Stage 3: the fault shear stress is set at the slip tendency. Stage 4: pre-injection permeability measurement. Stage 5: injection test and fault reactivation. Stage 6: post-reactivation permeability measurement. c) Double Direct Shear, DDS, experimental assemblages used during the experiments: standard characterization, top panel; injection test, bottom panel.

first has been conducted for the standard characterization (Fig. 3a) of the frictional strength and the rate and state (RSF) frictional parameters (healing rate and velocity dependence of friction, e.g., Dieterich, 1979; Ruina, 1983; Marone, 1998). The first type of experiments was carried to characterize the frictional properties of the fault at four different normal stresses (5, 15, 25, 35 MPa), which include the in-situ effective normal stress of 15 MPa. (e.g., Ma et al., 2022; Bröker and Ma, 2022). The sample is sheared at room temperature and at water-saturated conditions. These experiments consist of several stages listed here. Firstly, the samples are installed and saturated at low normal load of 0.5 MPa for 30 min. Then the normal stress is increased at steps of 0.5 MPa to the targeted normal stress, which is maintained constant throughout the experiment. After the attainment of a constant thinning rate, the sample is sheared for a total displacement of 7.5 mm at a slip rate of 10 μm/s (Fig. 3a). This stage is known as "run-in" and lets the fault to accommodate enough shear displacement to achieve a steady-state friction (Fig. 3a stage 1). The following stage, the slide-hold-slide series (SHS), consists of periods of hold, gradually increasing from 1 to 1000 s and separated by shearing phase of 500 μm at 10 μm/s (Fig. 3a, stage 2). The last stage consists of velocity steps in which the sample is sheared at increasing velocity, 0.3 to 300 μm/s, for 0.5 mm of shear displacement for each velocity step (Fig. 3a, stage 3).

Our characterization of frictional properties includes the steady-state frictional strength, the healing behavior in SHS tests, and velocity dependence of friction. We used the RSF friction theory (Dieterich, 1979; Ruina, 1983; Marone, 1998) as framework for our analysis. The friction coefficient, μ, is retrieved as the linear constant of proportionality between steady-state shear stress and normal stress, using Eq. (1):

$$\tau = \mu\sigma_n + c \quad (1)$$

where c is the cohesion term. During SHS test, the frictional healing ($\Delta\mu$) was obtained as the difference between the friction peak measured during re-shear following each hold and the steady state friction before the hold (Marone, 1998; Fig. 3a, stage 2). Frictional healing rate (β) was retrieved as the linear variation of $\Delta\mu$ with logarithm of the hold time (t_h).

$$\beta = \Delta\mu / log10(\Delta t_h) \quad (2)$$

In the velocity step tests, a quasi-instantaneous step in shear velocity from V_0 to V corresponds to a quasi-instantaneous variation of frictional strength which scales with a $\log_e(V/V_0)$, where a is an empirical parameter known as *direct effect* (Dieterich, 1979; Ruina, 1983). The subsequent evolution of friction to a new steady-state, scales with b $\log_e(V/V_0)$, where b is an empirical parameter known as *evolution effect* (Dieterich, 1979; Ruina, 1983; Fig. 3a stage 3). The a-b parameter,

which defines the velocity dependence of friction, is described by:

$$(a-b) = \Delta\mu_{ss}/log_e(V/V_0) \quad (3)$$

where $\Delta\mu_{ss}$ is the difference between the dynamic steady-state frictional strength after and before the step in shearing velocity from V_0 to V (Dieterich, 1979; Ruina, 1983). Negative value of (*a*-*b*) defines a velocity-weakening behavior, which is a required condition for the developing of frictional instability (Dieterich and Kilgore, 1994; Marone, 1998). Positive value of (*a*-*b*) defines a velocity-strengthening behavior, suggesting aseismic creep as the likely fault slip behavior. Each velocity step was modelled by using RSF equations (Eq. (4)) coupled with the Dieterich law (Eq. (5)), an evolution law that defines the state variable θ (Dieterich, 1979):

$$\mu = \mu_0 + a\, log_e(V/V_0) + b\, log_e(V_0\theta/D_c) \quad (4)$$

$$d\theta/dt = 1 - \theta V/D_c \quad (5)$$

where μ_0 is frictional strength at the steady state for slip velocity V_0, V is the frictional slip rate and D_c is the distance necessary to renew the population of asperities, the so-called *critical slip distance* (Dieterich, 1979, Ruina, 1983). The state variable, θ, is interpreted to represent the average lifetime of the asperities (Ruina, 1983). To model velocity steps, the previous two equations are coupled with another equation (Eq. (6)) which defines the elastic coupling between the sliding surface and the loading medium:

$$d\mu/dt = K(V_{lp} - V) \quad (6)$$

where V_{lp} is the loading point velocity and K is the stiffness normalized by normal stress (1/mm) of both the assembly and the loading apparatus (Saffer and Marone, 2003). These equations are solved simultaneously using a fifth order Runge-Kutta integration. *a*, *b*, and D_c were retrieved, for each velocity step, as best fit values using a, least squares iterative method to solve the inverse non-linear problem (Blanpied et al., 1998; Saffer and Marone, 2003).

3.1.2. Injection test

With the second type of experiments, we evaluated the fault slip behavior during hydraulic stimulation by fluid injection (Fig. 3). This experiment was performed in the pressure vessel at confining pressure $P_c = 15$ MPa, pore fluid pressure $P_f = 5$ MPa and initial effective normal stress of $\sigma'_n = 15$ MPa ($\sigma'_n = P_c + \Delta\sigma_n - P_f$, with $\Delta\sigma_n = 5$ MPa, details in Scuderi and Collettini, 2016). These values represent the in-situ stress conditions of the MC fault, where the measured pore-fluid pressure is about 5 MPa and the effective normal stress is about 15 MPa (Ma et al., 2022; Bröker and Ma, 2022). For this type of experiment, we used a different DDS assembly, consisting of three forcing blocks provided with channels to allow fluid to flow perpendicularly to the layers of gouge. The blocks are connected to the external fluid pressure intensifiers (Fig. 3c Lower panel) and equipped with grooved porous frits (permeability = 10^{-14} m^2). This assemblage ensures a homogenous fluid distribution on the entire surface of the sample, while forcing shear to be localized within the layers of gouge. For this configuration, the nominal frictional contact area is 55.4 by 55.5 mm, and the initial layer thickness is 5 mm (Fig. 3c lower panel). The whole sample assembly (i.e., the gouge layers and the forcing blocks) was separated from the confining oil by a rubber jacket (e.g., Scuderi and Collettini, 2016, 2018).

For this second type of experiments, we followed the procedures described by Scuderi and Collettini (2018). We began by applying the confining pressure, P_c, at steps of 1 MPa until reaching 5 MPa. Subsequently, we increased the normal stress by $\Delta\sigma_n = 5$ MPa (steps of 0.30 MPa), compacting the sample for 30 min. We then started applying the pore fluid pressure by increasing the upstream pressure (P_u) to 1 MPa and leaving the downstream lines open to the atmosphere until constant flow was attained through the assembly. After the full saturation of the gouge layers, we connected the downstream lines to the intensifier and waited for equilibration of the downstream pressure (P_d). Pore fluid pressure was then increased stepwise (1 MPa for each step) until the targeted pore fluid pressure was reached. The sample was left compacting to achieve a steady-state layer thickness.

After this preliminary stage, the sample was sheared at 10 μm/s of velocity for a total shear displacement of 10 mm ("run-in") letting the fault achieve a steady state shear stress, τ_{ss}, (Fig. 3b stage 1). We then stop the vertical piston to let the sample relax for 15 min and achieve a residual shear strength (Fig. 3b stage 2). This last stage is necessary to let the fault achieve an equilibrium porosity and an optimal fabric arrangement (e.g., Scuderi and Collettini, 2018). Thirdly, we set the fault to a constant shear stress of 5.25 MPa to match the in-situ state of stress inferred from slip tendency analysis (Ma et al., 2022), which is $\tau/\sigma'_n = 0.35$. Again, the sample was left to equilibrate for 45 min (Fig. 3b stage 3). Before starting the fluid injection, we performed a fault-perpendicular permeability test, using the constant head method (e.g., Ikari et al., 2009) (Fig. 3b stage 4), meaning 1 MPa of differential pressure (ΔP_f) was applied between P_u and P_d and the flow rate (Q) was monitored. Permeability (*k*) is obtained, using Darcy's law (Eq. (7)):

$$k = (Q\,\eta\,\Delta h)/(A\,\Delta P_f). \quad (7)$$

where Q is the average flow rate (m^3/s) across the gouge layer, calculated from the intensifier displacements over time multiplied by the intensifier cross section (0.0016 m^2), η is water viscosity (1.002×10^{-9} MPa s); Δh is the gouge layer thickness measured by LVDTs, A is the nominal area of the gouge layer (0.0030 m^2). Constant pressure difference was maintained until steady-state flow rate was achieved; this was assumed when the upstream and downstream flow rates were within 5% of each other and had reached a constant value (e.g., Ikari et al., 2009; Scuderi and Collettini, 2016, 2018). The injection test consisted of a stepwise increase of the fluid pressure, in agreement with the injection protocols designed for the MC fault stimulation: 0.2 MPa every 5 min (Fig. 3b stage 5). During the injection test, we monitored fault slip and fault layer thickness evolution. The test was stopped upon achievement of dynamic slip conditions (slip velocities >1 mm/s). After fault relaxation to a residual shear strength, we performed another permeability test to observe possible changes in permeability induced by the fault fabric evolution during reactivation (Fig. 3b stage 6).

3.1.3. Microstructural analysis

After each experiment, the deformed gouge layers were carefully extracted from the experimental assembly and prepared for the microstructural analysis following the procedures described by Volpe (Volpe et al., 2022b). The microstructural analysis of recovered microstructures was conducted on the kinematic section (e.g., Passchier, 1990; Volpe et al., 2022b). The microstructural imagery was obtained by a Field-Emission Scanning-Electron-Microscope (SEM) in back-scattered imaging mode (BSE).

4. Mechanical results

4.1. Frictional properties characterization

For all the considered normal stress conditions, the experimental fault displays a first stage of shear strengthening followed by a steady-state shear stress (Fig. 4a) which scale linearly with normal stress, indicating brittle behavior (Fig. 4b). These values are fitted by the Coulomb criterion, giving a friction coefficient, $\mu = 0.49 \pm 0.006$ (Fig. 4b), which is slightly below the Byerlee's range of friction ($0.6 < \mu_{ss} < 0.85$, Byerlee, 1978) and negligible cohesion (< 0.2 MPa). The frictional restrengthening scales linearly with the hold time, yielding healing rates, β, between 0.0039 and 0.0072 (Fig. 4c). Both $\Delta\mu$ and β values do not show any clear correlation with normal stress (Fig. 4c). The fault gouge shows a slight velocity strengthening to neutral

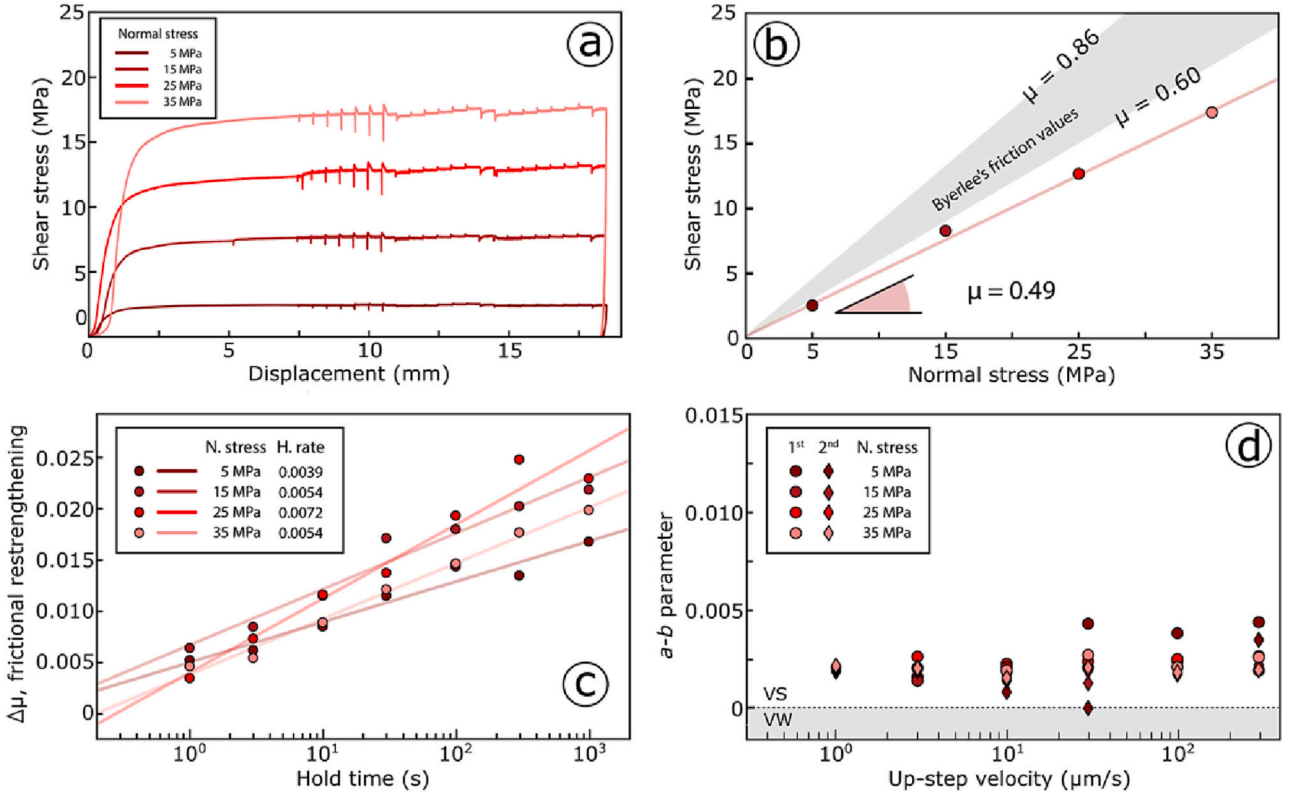

Fig. 4. experimental results from the standard frictional properties characterization of the gouge from the selected fault. a) raw data frictional curves in a shear stress – displacement plot; b) Mohr-Coulomb envelop of the gouge; c) frictional restrengthening in function of hold time, slopes represent the healing rate; d) velocity dependence of friction, VS: velocity strengthening behavior, VW: velocity weakening behavior (detailed summary of the experimental results can be found in the supporting information SI.3).

behavior for all the experiments with values ranging between ~0 and ~ 0.004 (Fig. 4d). The *a-b* parameter does not show any clear trend with shear velocity or normal stress (Fig. 4d). We do not observe any systematic variation of the *a-b* parameter for the two series of velocity steps, suggesting no evolution with strain.

4.2. Injection test (fault reactivation)

During the stage 1 of the experiment (Fig. 3b stage 1), we sheared the gouge for 10 mm at 15 MPa of effective normal stress until it attained a stable frictional strength of $\mu = 0.53$, consistent with the friction coefficient obtained from the Coulomb envelope at room pressure and water saturated conditions (Fig. 5a). During the injection phase (Fig. 3b stage 5), we evaluate the fault slip behavior. Fault slip evolved in a way similar to a trimodal creep behavior (e.g., Scuderi et al., 2017 and references therein; Fig. 5b and d). During the first ten steps of fluid pressure increase (up to $P_f = 15$ MPa, Fig. 3b), the fault displayed a decelerating creep, marked by the convex trend of the slip evolution curve (Fig. 5b). Successively, the fault showed a steady state creep with an average velocity of 3.5 nm/s (Fig. 5b and d). Accelerating creep was observed once the on-fault stress conditions crossed and overcame the Coulomb failure envelope (Fig. 5a, red arrow). At this point, the fault started sliding at increasing sliding velocity with an exponential evolution, mimicking a dynamic instability with velocities higher than 1 mm/s (Fig. 5d). At this velocity we stopped the experiment due to achievement of the maximum displacement of the piston. It is worth to emphasize that dynamic fault reactivation was not achieved when the state of stress reached the failure envelope (between yellow and red triangles in fig. 5a) but only when the fluid pressure was further raised by 1.2 MPa (six fluid injection steps), leading to fast slip acceleration.

During the fluid injection (stage 5 in Fig. 3b), we carefully monitored the evolution of the gouge layer thickness as a proxy for porosity and poroelastic response of the gouge (e.g., Samuelson et al., 2009; Fig. 5c). During the early phases of stage 5 (Fig. 3b), we documented an initial phase where the fault gouge undergone decelerating compaction (Fig. 5c) in correspondence of decelerating creep (Fig. 5b). During this phase, the fault compacted by ~2.5 μm (Fig. 5c). Dilation starts at the beginning of the steady-state creep (Fig. 5c). Through this stage the experimental fault dilated by ~2.5 μm (Fig. 5c). During the first part of the steady-state creep, the layer thickness evolution is characterized by a slight and gradual dilation (Fig. 5c). Successively, the evolution of the layer thickness is marked by a trend of dilation and compaction modulated by the steps of fluid injection (Fig. 5c and Agliardi et al., 2020). At each step, the gouge first dilates then gradually compacts (Fig. SI.5 in Supporting Information). This dilation-compaction behavior is observed below the fault's relaxation creep envelope ($\mu_c \sim 0.45$, Fig. 5a). Above the relaxation creep envelope, the initial dilation is followed by a secondary dilation at each step. This trend continues with incrementally faster dilation as the failure envelope is approached (Fig. 5c and Fig. SI.5 and SI.6 in Supporting Information). Once the on-fault stress conditions crossed the reactivation envelope, the fault started slipping into accelerating creep, during which dilation strongly accelerated and culminated with a total increment of 2.5 μm (from onset of accelerating creep, Fig. 5c). During the dynamic slip the fault rapidly compacted by ~1 mm (inset of Fig. 5c and Fig. SI.5 and SI.6 in Supporting Information).

4.3. Fault perpendicular permeability

Fault perpendicular permeability was measured before the injection phase and after the reactivation (Fig. 3b stage 4 and 6). The pre-injection permeability was 9.3×10^{-17} m^2. The post injection permeability

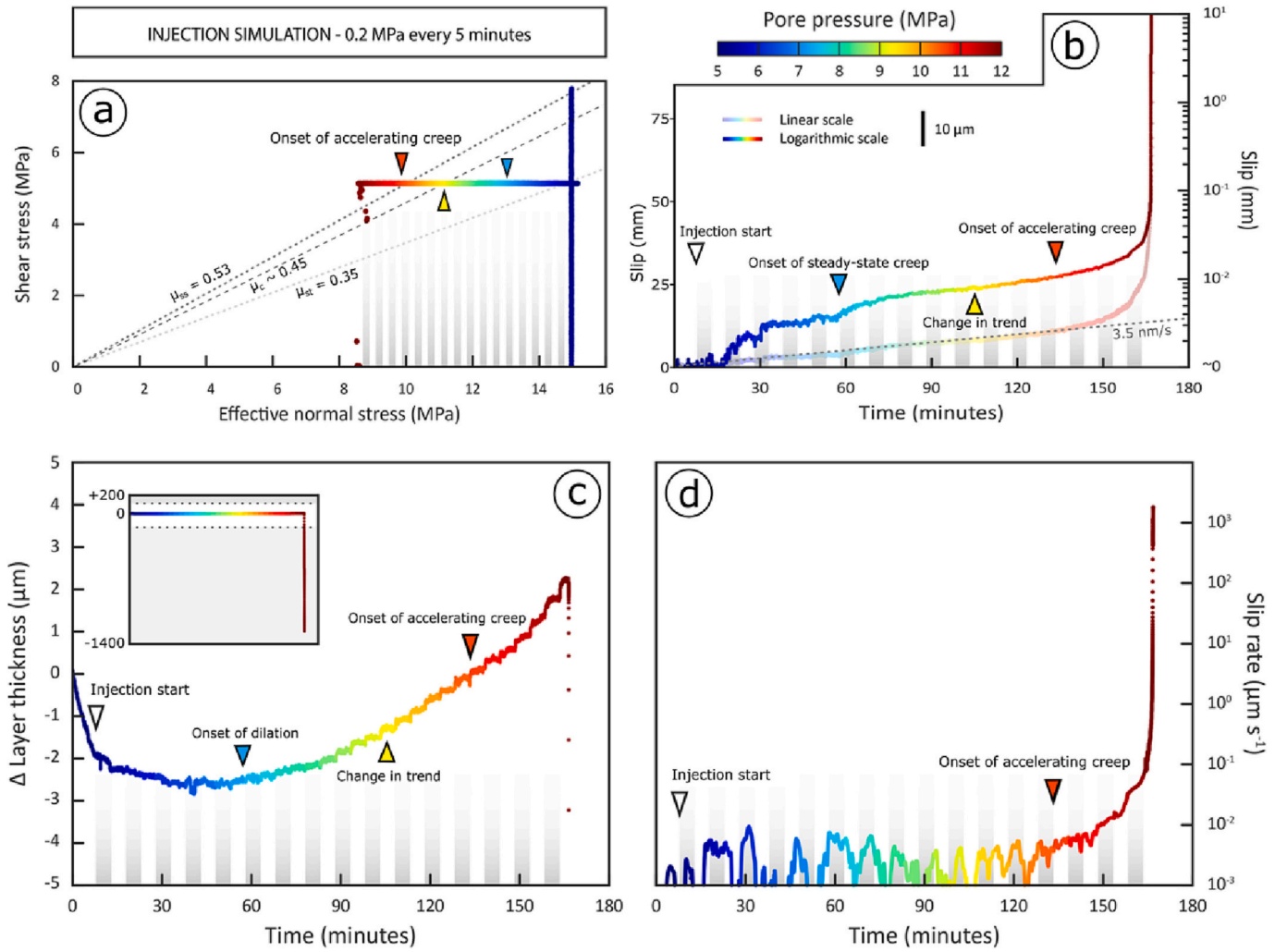

Fig. 5. experimental results from the injection experiment. a) evolution of effective normal stress and shear stress during the experiment. Frictional strength, μ_{ss}; slip tendency, μ_{st}; creep relaxation strength, μ_c (for further information see SI.4). b) Slip as function of time during the injection phase of the experiment (linear scale on left y-axis, logarithmic scale on right y-axis); c) variations of the gouge layer thickness during the injection phase (inset indicates the whole evolution of the gouge layer thickness during stage 5); d) slip rate as function of time during the injection phase. The triangles indicate major changes during the experiments. Note that triangles with same colour refer to the same intervals for all the panels. Gray and white vertical bands represent steps of fluid pressure.

measured just after fault reactivation (Fig. 3b stage 6) was about 2.9 × 10^{-17} m^2.

5. Experimental microstructures

The microstructural analysis was carried on the samples from the standard characterization experiments. Here we report those of the experiment performed at σ_n = 15 MPa, which represents the in-situ stress conditions (Fig. 6). The other microstructures are included in the Supporting Information (SI.7).

The deformed gouge at water saturated conditions shows the development of Y-B-P-R fabric (Logan, 1979; Volpe et al., 2022b) with severe grain-size reduction along localized shear zones (Fig. 6 a, b, c). The low strain domains (LSD) are almost undeformed and display a grain size close to the original (~125 μm), observable within the indentations (Fig. 6a, b, c). The deformation is mainly localized along a single comminuted zone, the principal slipping zone, localized at the slider block boundary (e.g., Fig. 6a, b). R (Riedel) and P (compressive) shear zones are evidenced by opened fractures induced by decompression (Fig. 6a, b; Volpe et al., 2022b) and are localized within the principal slip zone. At higher magnification, the principal slipping zone contains fractured grains characterized by a heterogeneous shape and size, often mantled by phyllosilicates. Oriented platelets of biotite produce a weak s-foliation (proto-foliation, e.g., Giorgetti et al., 2015; Volpe et al., 2022b) oriented favorably with the direction of shear (Fig. 6c, d, e). The microstructure suggests deformation dominated by cataclastic processes (fracturing, grain-size reduction, and frictional sliding along grain boundaries, e.g., Sibson, 1977) supported by the grain load-bearing framework made by the granular fraction (e.g., quartz, feldspars in Fig. 6c, d). Minor frictional sliding along foliation may occur along the phyllosilicates proto-foliation (Fig. 6d, e).

6. Discussions

6.1. Mineralogy, fabric, and frictional properties

Mineralogy, fabric, and frictional properties have been analyzed to define key aspects of the mechanical behavior of the MC fault to understand fault suitability for the activities of the FEAR project. Our analysis focused on the fine gouge fraction collected in-situ from the MC fault core. We followed this approach since gouge bearing faults seem to be the most common character for brittle faults within the Bedretto tunnel and therefore those that should experience fluid induced reactivation during the FEAR activities.

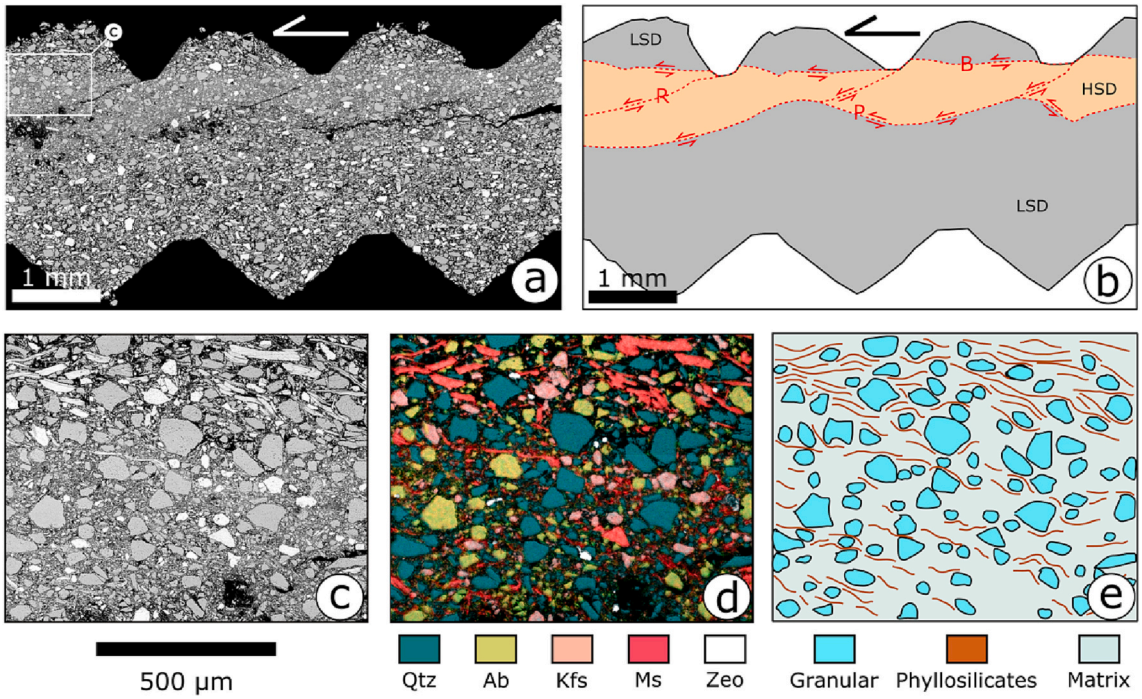

Fig. 6. Microstructural characterization of experimental post-mortem gouge. a) panoramic view of the deformed gouge at 15 MPa (arrows mark the direction of shear); b) microstructural interpretation of panel a: low strain domains in gray and high strain domains in orange are shown. In the high strain domains, the structural features are labeled according to the Logan (1979) nomenclature (Y-P-B-R). c) close-up of the principal shear zone (white box in panel a); d) Energy Dispersive X-ray Spectroscopy (EDS) map of the principal shear zone in panel c showing granular and sheet silicates minerals; e) schematic microstructural line drawing of the principal shear zone.

Microstructural analysis of the in-situ samples shows a discrete layer (< 5 mm) of extremely comminuted minerals, which have been segregated from the coarser and angular cataclasite by sieving (< 125 μm). The mechanical behavior of this material has been characterized with laboratory friction experiments.

The gouge deformed at 10 μm/s deforms with a steady state friction coefficient of $\mu \approx 0.49$. The stress values plotted in a normal stress vs. shear stress diagram, are distributed in a straight line concordant with the Coulomb criterion (Fig. 4b) and indicative of a deformation mainly controlled by the frictional properties of fault rock. With slide-hold-slide tests we observed moderate to high healing rates ($0.0032 < \beta < 0.0072$) and velocity neutral or slightly velocity strengthening behavior is documented with velocity stepping tests (Fig. 4). These results are consistent with data from studies on gouge with similar mineral assemblages (Tembe et al., 2010; Ikari et al., 2011; Volpe et al., 2022b), which consisted of a mixture of abundant granular minerals (quartz and feldspars, 78%) and phyllosilicates (muscovite with minor chlorite and biotite; 22%). The high quartz and feldspar content allows for the development of a load-bearing granular framework which supports most of the deformation (Fig. 6c). Indeed, moderately high friction and healing rates suggest that the main deformation mechanism is cataclasis (e.g., Sibson, 1977; Marone and Scholz, 1988; Scholz, 2019). Positive healing corresponds to growth of contact area at asperities (grain contact junction) with hold time (Dieterich and Kilgore, 1994; Marone, 1998). However, the slightly lower values of friction and healing rates compared to those measured on granite powders with similar composition (e.g., Carpenter et al., 2016) can be interpret as the result of the influence of sheet silicates in the fine fraction of the MC fault gouge. Furthermore, the MC fault gouge presents slightly positive *a-b* values, different from the rate-weakening behavior expected for granite bare surfaces and gouges (e.g., Marone et al., 1990; Ikari et al., 2011). This interpretation is supported by microstructures that depicts a fabric within the principal shear zone, where the granular fraction is weakly affected by grain-size reduction and is discontinuously embedded and mantled by the more comminuted phyllosilicate-rich matrix (Fig. 5d, e). This suggests that cataclasis is the main deformation mechanism, but also that part of the deformation is accommodated by frictional sliding along the phyllosilicates foliae, thus reducing hard interaction within granular fraction (e.g., Saffer and Marone, 2003; Collettini et al., 2009; Niemeijer et al., 2010; Giorgetti et al., 2015; Volpe et al., 2022b).

These microstructures shed light on the interpretation of the experimentally measured fault permeability. The gouge, in the injection experiment, displayed a fault perpendicular permeability in the order of 10^{-17} to 10^{-16} m^2. These values are in agreement with the permeability of gouges of similar mineralogical composition tested at similar boundary conditions (e.g., Crawford et al., 2008; Ikari et al., 2009). Purely granular gouges display values of permeability generally higher than 10^{-16} m^2 (e.g., Crawford et al., 2008). It is in fact known that fault gouge permeability decreases with increasing phyllosilicate content (e.g., Saffer and Marone, 2003; Crawford et al., 2008; Ikari et al., 2009). In our case, the phyllosilicate content (22%) is sufficiently high to promote such a permeability reduction. We also measured permeability before and after the injection phase (Fig. 3b stage 4 and 6), yielding a permeability of $9.32*10^{-17}$ m^2 (10 mm of slip) and 2.91×10^{-17} m^2 (20 mm of slip), respectively. We interpret this as the effect of grain size reduction and porosity decrease of the PSZ with increasing strain (e.g., Faulkner and Rutter, 2003; Ikari et al., 2009; Scuderi et al., 2017), accumulated especially during the dynamic reactivation phase (10 mm). Incremental deformation may also favor interconnection of the phyllosilicate matrix, resulting in similar observations (e.g., Fig. 6c, d, e, e.g., Ikari et al., 2009). Notably, the yielded permeability values agree with the in-situ permeability measurements made on faults within similar crystalline rocks (Shapiro et al., 1997; Achtziger-Zupančič et al., 2017; Schoenball et al., 2018).

6.2. *Fault slip behavior during pressurization*

During stage 1 of the injection test (Fig. 3b), the gouge attained a

frictional strength concordant with the frictional strength obtained from the Coulomb envelope at room pressure and water saturated conditions (Fig. 4b and Fig. 5a). During stage 5 of the experiment (Fig. 3b), the fault exhibited the typical trimodal creep behavior which has been previously described (e.g., Scuderi et al., 2017 and references therein). The first phase is associated with decelerating creep and lasted nine steps of fluid injection (corresponding to a pore fluid pressure increase of 1.8 MPa). Throughout decelerating creep, the fault is characterized by gradual compaction due to fabric rearrangement favored by closure of small cracks and changes in grain arrangement (e.g., Samuelson et al., 2009; Ikari et al., 2009; Scuderi et al., 2017). Here, the gouge reached a stationary layer thickness that corresponds to a steady state porosity and fabric (e.g., Marone and Scholz, 1988; Ikari et al., 2009, 2011; Scuderi et al., 2017). This stationary layer thickness resulted also from the balance between fluid injection induced dilatancy and the overall gouge compaction (e.g., Scuderi and Collettini, 2018 and Fig. SI.5 in Supporting Information). The second phase is associated to steady-state creep, during which the fault slides at a nearly constant velocity of ~3.5 nm/s (Fig. 5d). This creeping velocity is in the range of the steady-state creep velocity observed for granular-rich gouges (carbonates) in similar creep experiments (Scuderi et al., 2017). The onset of steady-state creep occurred in correspondence of the onset of dilation (Fig. 5c and Fig. SI.5 and SI.6 in Supporting Information). During the steady-state creep the fault crossed its creep relaxation envelope ($\mu = 0.45$, Fig. 5a). In correspondence to the crossing point, we observed a gentle increase in sliding velocity as well as a change in layer thickness evolution: from dilation-compaction modulated by fluid injection to continuous dilation (higher upon pressurization; lower following the pressurization step e.g., Fig. 5c and Fig. SI.5 in Supporting Information). Similar correspondence between layer thickness evolution and fault slip behavior was already observed in other works (e.g., French et al., 2016; Scuderi et al., 2017 and Scuderi and Collettini, 2018 and Fig. SI.6 in Supporting Information). As the stress state of the experimental fault crossed the failure envelope (Fig. 5a), the fault entered into accelerating creep phase, throughout which the gouge started sliding at increasing velocity, still strongly dilating (Fig. 5c). Further fluid injections promoted an exponential increase in fault slip velocity that resulted in dynamic frictional instability; during the dynamic reactivation the gouge dramatically compacted (Fig. 5c). The dynamic reactivation occurred at an effective normal stress of 8.4 MPa, that corresponds to a frictional strength of $\mu = 0.61$ for the imposed constant shear stress of 5.25 MPa (Fig. 5a). This frictional strength value is 0.12 above the laboratory measured Coulomb envelope ($\mu = 0.49 \pm 0.006$, Fig. 5a) corresponding to 0.9 MPa of shear stress above the reactivation criterion at the same normal stress. Several processes can act together to promote reactivation at higher frictional strength. These include, but are not limited to, the healing properties of the material (Fig. 4c), the slightly velocity strengthening behavior of the fault rock (Fig. 4d), the short time between fluid pressure steps not allowing the accelerating creep to evolve into a dynamic instability, and non-uniform pore fluid pressure distribution within the experimental fault (e.g., Passelègue et al., 2020).

6.3. *Implications for fault reactivation and induced seismicity in the BedrettoLab*

Rock deformation experiments, aimed at reproducing the injection protocol designed for the reactivation of the MC fault within the Bedretto laboratory, show that the MC fault can produce an earthquake instability upon pressurization. This instability occurs (Fig. 5b and d) even though the fault rock is characterized by a slightly velocity strengthening/velocity neutral behavior (Fig. 4d), and therefore within the rate and state frictional framework should experience stable sliding and fault creep (e.g., Marone and Scholz, 1988; Marone, 1998). Our interpretation for this behavior is that during fluid pressure stimulation, the weakening induced by the increase of fluid pressure is higher than the velocity strengthening behavior of the material, and therefore a dynamic frictional instability is promoted. Similar results have been observed in other laboratory experiments, suggesting that changes in pore fluid pressure may overcome the frictional changes forecasted by classical RSF friction laws, hence exerting a strong influence on nucleation of earthquakes (Sawai et al., 2016; French et al., 2016; Scuderi et al., 2017; Proctor et al., 2020).

Can we expect the same slip behavior for the natural MC fault within the Bedretto tunnel? To address this question, it is important to emphasize that our experiments reproduced ideal conditions, where the fault has a finite lateral extension and is characterized by homogeneous gouge distribution. These conditions allow a strong and direct control on the stress state (e.g., shear stress, normal stress, and fluid pressure), fault evolution (dilation/compaction, slip) within each phase of the experiment. In addition, we can supply a constant distribution of fluid pressure along the entire fault and induced fluid pressure steps that were distributed homogeneously throughout the entire fault structure. Within the natural MC fault, it is unrealistic to expect boundary conditions similar to those well-constrained in laboratory experiments. For example, lithological heterogeneities and multiple fault surfaces may affect stress distribution, and/or the widespread fracture system associated to the MC fault might limit the fluid pressure pulse to a restricted area. In other words, it will be difficult if not impossible to pressurize the entire MC fault in the same way of the 5x5cm wide experimental fault pressurized in our laboratory tests.

Despite these important differences we think that the laboratory experiments can provide important insights into the hydromechanical coupling of the fault during fluid pressure stimulation and increase interpretability of the results once the MC fault will be stimulated in the BedrettoLab. From our rock deformation experiments we depicted two end-members scenarios for fluid pressure induced MC fault reactivation.

In the first case, the pressurization rate is high enough to bring the stress state of the fault beyond the failure envelope (Fig. 7, red curve). This case can be also achieved for high injection rates, largely exceeding the hydraulic diffusivity of the fault zone, especially in the case of low fault permeability values (i.e., Rutter and Hackston, 2017; Passelègue et al., 2018, 2020; Wang et al., 2020; Ji et al., 2022a). Here, the weakening induced by fluid pressurization is sufficient to exceed the moderate velocity strengthening behavior of the gouge, and therefore promotes earthquake slip (e.g., Sawai et al., 2016; Scuderi et al., 2017; Proctor et al., 2020). This scenario is assimilable with what we observed in our rock deformation experiments (Fig. 5a) with the exception that, in laboratory experiments the shear stress is maintained constant until the onset of dynamic instability (Fig. 7, blue curve), whereas in the natural case, slip accommodated along the fault relieves progressively the shear stress. The load control of injection tests i.e., constant shear stress, prevents the reproduction of this behavior in rock deformation experiments in its entity, (Fig. 7, blue curve). In the second case, the fracture system associated to the MC fault (as well as newly developed fractures) results in an overall high permeability that prevents significant fluid pressure to induce fault weakening, i.e., a reduction of the effective normal stress significantly beyond the failure envelope (Fig. 7, green curve). This case is also valid when a lower injection rate is applied to relatively lower permeabilities (i.e., French et al., 2016; Rutter and Hackston, 2017; Passelègue et al., 2018, 2020; Wang et al., 2020; Ji et al., 2022b). For these boundary conditions, our laboratory results predict that weakening induced by fluid pressure build-up is counteracted by the slight velocity strengthening behavior of the fault gouge and therefore fault creep or accelerated fault creep is the most likely slip behavior (Fig. 7, green curve). However, even in the second case, continued and accelerated creep may increase shear stress at the edges of the creeping zone and trigger instabilities (e.g., Guglielmi et al., 2015; Cappa et al., 2019) even on faults with a moderate velocity strengthening behavior (e.g., Boatwright and Cocco, 1996). This second case was recently recorded during hydraulic fracturing activities in Alberta, Canada (Eyre et al., 2019), where the accelerated creep, produced by the hydraulic stimulations of strongly velocity strengthening clay-rich

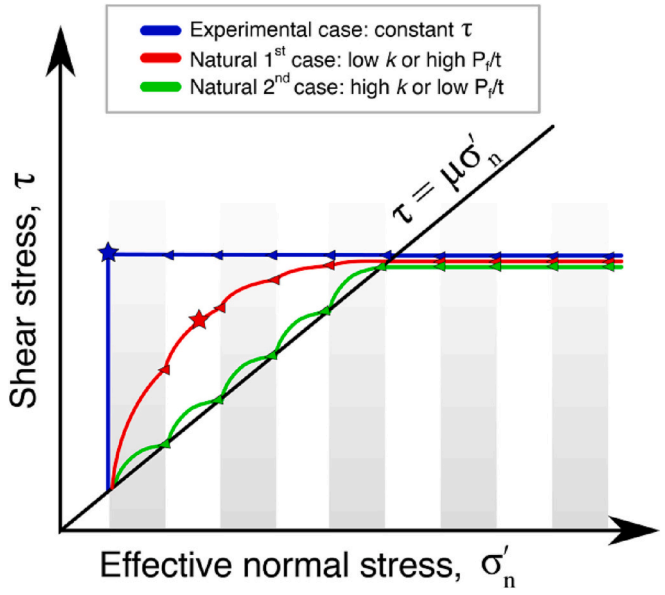

Fig. 7. Schematic evolution of the stress state during reactivation. Blu curve shows the experimental case where the shear stress is maintained constant until abrupt fault dynamic reactivation (blue star). Red curve represents the first scenario, where either the natural fault has low permeability (low *k*) or the injection rates (high P_f/t) are high enough to allow fluid pressure build-up beyond the failure envelope and promote earthquake slip (red stars). Green curve represents the second scenario where the high permeability of the natural fault (high *k*) or low injection rates (low P_f/t) prevents fluid pressure build-up significantly beyond the failure envelope favoring fault creep or accelerated fault creep as the most likely slip behavior. Gray and white vertical bands represent steps of fluid pressure. Note that the figure is not in scale and stress paths have been exaggerated for representation purposes. (For interpretation of the references to colour in this figure legend, the reader is referred to the web version of this article.)

lithologies (Scuderi and Collettini, 2018), promoted an increase of stress along neighboring faults contained within carbonatic rocks where earthquakes nucleated (Eyre et al., 2019).

7. Conclusions

In this work, we have used structural geology and rock deformation experiments to characterize the main branch of the MC fault which has been selected to be reactivated via fluid pressure stimulations within the BedrettoLab (Switzerland). The MC fault is an old structure that accommodated deformation in the ductile field and was successively reactivated within the brittle field. The latter is testified by a narrow fault core with the presence of an unconsolidated, cataclastic fault gouge made of 78% of granular silicates (quartz, feldspars, and zeolites) and 22% of phyllosilicates (micas). Standard rock deformation frictional experiments conducted on the MC fault gouge depict a fault characterized by relatively high friction ($\mu = 0.49 \pm 0.006$), moderate/high healing rate and a moderate velocity strengthening/neutral behavior. Experiment designed to evaluate the slip behavior of the fault during fluid pressure stimulations shows that once the stress state approaches the failure envelope the fault starts to creep. For further weakening induced by fluid pressure builds-up, the fault experiences a dynamic instability irrespective of the rate-strengthening behavior of the gouge. We interpret that the fluid pressurization induced weakening overcomes the slightly rate strengthening behavior of the gouge promoting a laboratory earthquake during fluid pressure stimulation.

Despite the important differences in boundary conditions between fluid-induced fault reactivation in rock deformation experiments and the natural MC fault in the Bedretto underground laboratory, rock deformation tests provide important insights to predict the slip behavior of the natural MC fault. We envision two possible end-member scenarios for the slip behavior of the MC fault during pressurization: In a first case, similar to rock deformation experiments, fluid injection remains localized and therefore fluid overpressure increments, in particular if they occur in short time, promote the weakening required to develop an earthquake instability. In the second case, the fracture system associated to the MC fault favors high permeability that prevent significant fluid pressure induced fault weakening. In this second case the weakening induced by fluid pressure build-up is counteracted by the slightly velocity strengthening behavior of the gouge and therefore fault creep is the most likely slip behavior. In this case, earthquakes are triggered by a possible increase of shear stress at the edges of the creeping zone. The reactivation of the MC fault in the Bedretto tunnel will be a unique opportunity to test these hypotheses, revisit the interpretations of fault slip behaviors and better address further research activities on induced seismicity and in general on earthquake physics. The results of the current study contribute to fill the gap between laboratory measurements on experimental faults and observations at the BedrettoLab-scale on a natural fault.

CRediT authorship contribution statement

G. Volpe: Data curation, Investigation, Writing – original draft, Writing – review & editing. **G. Pozzi:** Data curation, Investigation, Supervision, Writing – original draft, Writing – review & editing. **C. Collettini:** Funding acquisition, Resources, Supervision, Writing – review & editing. **E. Spagnuolo:** Supervision, Writing – review & editing. **P. Achtziger-Zupančič:** Investigation, Writing – review & editing. **A. Zappone:** Supervision, Writing – review & editing. **L. Aldega:** Investigation, Writing – review & editing. **M.A. Meier:** Supervision, Writing - review & editing. **D. Giardini:** Project administration, Funding acquisition, Supervision, Writing – review & editing. **M. Cocco:** Funding acquisition, Project administration, Supervision, Writing – original draft, Writing – review & editing.

Declaration of Competing Interest

The authors declare that they have no known competing financial interests or personal relationships that could have appeared to influence the work reported in this paper.

Data availability

Experimental data files are available at https://doi.org/10.5281/zenodo.7410958

Acknowledgements

We thank the BedrettoLab team to give us the opportunity to work in the tunnel. We also thank D. Mannetta for his help with thin sections preparation and M. Nazzari for the support at the SEM-INGV laboratory. This study has received funding from the European Research Council (ERC) under the European Union's Horizon 2020 research and innovation program. M. Cocco and D. Giardini participated in this work as Principal Investigators of the Horizon 2020 ERC project FEAR (grant 856559). G. Pozzi, E. Spagnuolo, P. Achtziger-Zupančič, A. Zappone and M.A. Meier participated in this work in the framework of the ERC project FEAR. We thank A. Ceccato and the FEAR Geology Working Group for providing information and helpful discussion. This research was also supported by ERC grant Nr. 259256 GLASS and Ateneo 2018 to C. Collettini. We also thank J. Mecklenburgh, Yinlin Ji, and an anonymous Reviewer for their constructive reviews that increase the quality of the manuscript.

Appendix A. Supplementary data

Supplementary data to this article can be found online at https://doi.org/10.1016/j.tecto.2023.229987.

References

Achtziger-Zupančič, P., Loew, S., Mariethoz, G., 2017. A new global database to improve predictions of permeability distribution in crystalline rocks at site scale. J. Geophys. Res. Solid Earth 122 (5), 3513–3539.

Agliardi, F., Scuderi, M.M., Fusi, N., Collettini, C., 2020. Slow-to-fast transition of giant creeping rockslides modulated by undrained loading in basal shear zones. Nat. Commun. 11 (1), 1–11.

Arnet, M., 2021. Deep Alpine Fluids: Origin, Pathways and Dynamic Remobilisation in Response to Hydraulic Stimulations at the Bedretto Underground Laboratory for Geoenergies (BULGG) (Master's Thesis).

Blanpied, M.L., Marone, C.J., Lockner, D.A., Byerlee, J.D., King, D.P., 1998. Quantitative measure of the variation in fault rheology due to fluid-rock interactions. J. Geophys. Res. Solid Earth 103 (B5), 9691–9712.

Boatwright, J., Cocco, M., 1996. Frictional constraints on crustal faulting. J. Geophys. Res. Solid Earth 101 (B6), 13895–13909.

Bröker, K., Ma, X., 2022. Estimating the least principal stress in a granitic rock mass: systematic mini-frac tests and elaborated pressure transient analysis. Rock Mech. Rock. Eng. 55 (4), 1931–1954.

Byerlee, J., 1978. Friction of rocks. Pure Appl. Geophys. 116, 615–626.

Cappa, F., Scuderi, M.M., Collettini, C., Guglielmi, Y., Avouac, J.P., 2019. Stabilization of fault slip by fluid injection in the laboratory and in situ. Sci. Adv. 5 (3) eaau4065.

Carpenter, B.M., Ikari, M.J., Marone, C., 2016. Laboratory observations of time-dependent frictional strengthening and stress relaxation in natural and synthetic fault gouges. J. Geophys. Res. Solid Earth 121 (2), 1183–1201.

Ceccato, A., Behr, W.M., Zappone, A.S., 2023. The Mechanical Evolution of the European Continental Crust through the Alpine Orogenic Cycle: Insights from the Rotondo Granite (Gotthard massif, Central Swiss Alps) (No. EGU23-8225). Copernicus Meetings.

Collettini, C., Niemeijer, A., Viti, C., Marone, C.J., 2009. Fault zone fabric and fault weakness. Nature 462, 907–910.

Collettini, C., Di Stefano, G., Carpenter, B., Scarlato, P., Tesei, T., Mollo, S., Trippetta, F., Marone, C., Romeo, G., Chiaraluce, L., 2014. A novel and versatile apparatus for brittle rock deformation. Int. J. Rock Mech. Min. Sci. 66, 114–123.

Crawford, B.R., Faulkner, D.R., Rutter, E.H., 2008. Strength, porosity, and permeability development during hydrostatic and shear loading of synthetic quartz-clay fault gouge. J. Geophys. Res. Solid Earth 113 (B3).

Diehl, T., Clinton, J., Deichmann, N., Cauzzi, C., Kästli, P., Kraft, T., Molinari, I., Bose, M., Michel, C., Hobiger, M., Haslinger, F., Fah, D., Wiemer, S., 2018. Earthquakes in Switzerland and surrounding regions during 2015 and 2016. Swiss J. Geosci. 111 (1), 221–244.

Dieterich, J.H., 1979. Modeling of rock friction 1. Experimental results and constitutive equations. J. Geophys. Res., Solid Earth 84, 2161–2168. https://doi.org/10.1029/JB084iB05p02161.

Dieterich, J.H., Kilgore, B.D., 1994. Direct observation of frictional contacts: new insights for state-dependent properties. Pure Appl. Geophys. 143, 283–302.

Eyre, T.S., Eaton, D.W., Garagash, D.I., Zecevic, M., Venieri, M., Weir, R., Lawton, D.C., 2019. The role of aseismic slip in hydraulic fracturing–induced seismicity. Sci. Adv. 5 (8) eaav7172.

Faulkner, D.R., Rutter, E.H., 2003. The effect of temperature, the nature of the pore fluid, and subyield differential stress on the permeability of phyllosilicate-rich fault gouge. J. Geophys. Res. Solid Earth 108 (B5).

French, M.E., Zhu, W., Banker, J., 2016. Fault slip controlled by stress path and fluid pressurization rate. Geophys. Res. Lett. 43 (9), 4330–4339.

Giorgetti, C., Carpenter, B.M., Collettini, C., 2015. Frictional behaviour of talc-calcite mixtures. J. Geophys. Res. Solid Earth 120. https://doi.org/10.1002/2015JB011970.

Guglielmi, Y., Cappa, F., Avouac, J.P., Henry, P., Elsworth, D., 2015. Seismicity triggered by fluid injection–induced aseismic slip. Science 348 (6240), 1224–1226.

Hafner, S., 1958. Petrographie des südwestlichen Gotthardmassivs zwischen St. Gotthardpass und Nufenenpass. Doctoral dissertation. ETH Zurich.

Heidbach, O., Rajabi, M., Cui, X., Fuchs, K., Müller, B., Reinecker, J., Reiter, K., Tingay, M., Wenzel, F., Xie, F., Ziegler, M.O., Zoback, M.-L., Zoback, M., 2018. The World Stress Map database release 2016: Crustal stress pattern across scales. Tectonophysics 744, 484–498. https://doi.org/10.1016/j.tecto.2018.07.007.

Ikari, M.J., Saffer, D.M., Marone, C., 2009. Frictional and hydrologic properties of clay-rich fault gouge. J. Geophys. Res. Solid Earth 114 (B5).

Ikari, M.J., Marone, C., Saffer, D.M., 2011. On the relation between fault strength and frictional stability. Geology 39 (1), 83–86.

Ji, Y., Hofmann, H., Rutter, E.H., Zang, A., 2022a. Transition from slow to fast injection-induced slip of an experimental fault in granite promoted by elevated temperature. Geophys. Res. Lett. 49 (23) e2022GL101212.

Ji, Y., Wang, L., Hofmann, H., Kwiatek, G., Dresen, G., 2022b. High-Rate Fluid Injection Reduces the Nucleation Length of Laboratory Earthquakes on Critically Stressed Faults in Granite. Geophysical Research Letters 49 (23), e2022GL100418.

Jordan, D., 2019. Geological Characterization of the Bedretto Underground Laboratory for Geoenergies. Master's thesis. ETH Zurich, Geological Institute.

Kastrup, U., Zoback, M.L., Deichmann, N., Evans, K.F., Giardini, D., Michael, A.J., 2004. Stress field variations in the Swiss Alps and the northern Alpine foreland derived from inversion of fault plane solutions. J. Geophys. Res. Solid Earth 109 (B1).

Keller, F., Schneider, T.R., 1982. Geologie und Geotechnik. Schweiz. Ing. Architekt 100 (24), 512–520.

Labhart, T., 2005. Erläuterungen Zum Geologischen Atlas Des Schweiz 1: 25 000. Val Bedretto, Atlasblatt, Vol. 68.

Logan, J.M., 1979. Experimental studies of simulated gouge and their application to studies of natural fault zones. In: Proceedings of Conference VIII-Analysis of Actual Fault Zones in Bedrock, pp. 305–343.

Lützenkirchen, V.H., 2002. Structural Geology and Hydrogeology of Brittle Fault Zones in the Central and Eastern Gotthard Massif, Switzerland. Doctoral dissertation. ETH Zurich.

Lützenkirchen, V., Loew, S., 2011. Late Alpine brittle faulting in the Rotondo granite (Switzerland): deformation mechanisms and fault evolution. Swiss J. Geosci. 104 (1), 31–54.

Ma, X., Hertrich, M., Amann, F., Bröker, K., Gholizadeh Doonechaly, N., Gischig, V., Hochreutener, R., Kastli, P., Krietsch, H., Marti, M., Nageli, B., Nejati, M., Obermann, A., Plenkers, K., Rinaldi, A.P., Shakas, A., Villiger, L., Wenning, Q., Zappone, A., Bethmann, F., Castilla, R., Seberto, F., Meier, P., Driesner, T., Loew, S., Maurer, H., Saar, M.O., Wiemer, S., Giardini, D., 2022. Multi-disciplinary characterizations of the BedrettoLab–a new underground geoscience research facility. Solid Earth 13 (2), 301–322.

Marone, C., 1998. Laboratory-derived friction laws and their application to seismic faulting. Annu. Rev. Earth Planet. Sci. 26, 643–696. https://doi.org/10.1146/annurev.earth.26.1.643.

Marone, C., Scholz, C.H., 1988. The depth of seismic faulting and the upper transition from stable to unstable slip regimes. Geophys. Res. Lett. 15 (6), 621–624.

Marone, C., Raleigh, C.B., Scholz, C.H., 1990. Frictional behavior and constitutive modeling of simulated fault gouge. J. Geophys. Res. Solid Earth 95 (B5), 7007–7025.

Moore, D.M., Reynolds Jr., R.C., 1997. X-Ray Diffraction and the Identification and Analysis of Clay Minerals. Oxford University Press, Oxford, UK, 378 pp.

Nakatani, M., Yabe, Y., Philipp, J., Morema, G., Stanchits, S., Dresen, G., 2008. Acoustic emission measurements in a deep gold mine in South Africa: Project overview and some typical waveforms. In: SSA Annual Meeting 2008 (Santa Fe, New Mexico 2008).

Niemeijer, A., Marone, C., Elsworth, D., 2010. Fabric induced weakness of tectonic faults. Geophys. Res. Lett. 37 (3).

Ofterdinger, U.S., 2001. Ground Water Flow Systems in the Rotondo Granite, Central Alps (Switzerland). Doctoral dissertation, ETH Zurich.

Passchier, C.W., 1990. A Mohr circle construction to plot the stretch history of material lines. J. Struct. Geol. 12 (4), 513–515.

Passelègue, F.X., Brantut, N., Mitchell, T.M., 2018. Fault reactivation by fluid injection: controls from stress state and injection rate. Geophys. Res. Lett. 45 (23), 12–837.

Passelègue, F.X., Almakari, M., Dublanchet, P., Barras, F., Fortin, J., Violay, M., 2020. Initial effective stress controls the nature of earthquakes. Nat. Commun. 11 (1), 5132.

Proctor, B., Lockner, D.A., Kilgore, B.D., Mitchell, T.M., Beeler, N.M., 2020. Direct evidence for fluid pressure, dilatancy, and compaction affecting slip in isolated faults. Geophys. Res. Lett. 47 (16) e2019GL086767.

Rast, M., 2020. Geology, Geochronology, and Rock Magnetics along Bedretto Tunnel (Gotthard Massif, Central Alps) and Numerical Modelling of Quartz-Biotite Aggregates-Appendix a.

Rast, M., Galli, A., Ruh, J.B., Guillong, M., Madonna, C., 2022. Geology along the Bedretto tunnel: kinematic and geochronological constraints on the evolution of the Gotthard Massif (Central Alps). Swiss J. Geosci. 115 (1), 1–31.

Reches, Z.E., 2006. Building a natural earthquake laboratory at focal depth (DAFSAM-NELSAM Project, South Africa). Sci. Drill. 3, 30–33.

Ruina, A., 1983. Slip instability and state variable friction laws. J. Geophys. Res. 88, 10359–10370. https://doi.org/10.1029/JB088iB12p10359.

Rutter, E., Hackston, 2017. A. On the effective stress law for rock-on-rock frictional sliding, and fault slip triggered by means of fluid injection. Philos. Trans. A Math. Phys. Eng. Sci. 375 https://doi.org/10.1098/rsta.2016.0001, 20160001.

Saffer, D.M., Marone, C., 2003. Comparison of smectite-and illite-rich gouge frictional properties: application to the updip limit of the seismogenic zone along subduction megathrusts. Earth Planet. Sci. Lett. 215 (1–2), 219–235.

Samuelson, J., Elsworth, D., Marone, C., 2009. Shear-induced dilatancy of fluid-saturated faults: Experiment and theory. J. Geophys. Res. Solid Earth 114 (B12).

Sawai, M., Niemeijer, A.R., Plümper, O., Hirose, T., Spiers, C.J., 2016. Nucleation of frictional instability caused by fluid pressurization in subducted blueschist. Geophys. Res. Lett. 43 (6), 2543–2551.

Schneider, T.R., 1985. Basistunnel Furka—Geologische Aufnahme des Fensters Bedretto. Brig, Furka-Oberalp-Bahn AG.

Schoenball, M., Walsh, F.R., Weingarten, M., Ellsworth, W.L., 2018. How faults wake up: the Guthrie-Langston, Oklahoma earthquakes. Lead. Edge 37 (2), 100–106.

Scholz, C.H., 2019. The Mechanics of Earthquakes and Faulting. Cambridge University Press.

Scuderi, M.M., Collettini, C., 2016. The role of fluid pressure in induced vs. triggered seismicity: Insights from rock deformation experiments on carbonates. Sci. Rep. 6 (1), 1–9.

Scuderi, M.M., Collettini, C., 2018. Fluid injection and the mechanics of frictional stability of shale-bearing faults. J. Geophys. Res. Solid Earth 123 (10), 8364–8384.

Scuderi, M.M., Collettini, C., Marone, C., 2017. Frictional stability and earthquake triggering during fluid pressure stimulation of an experimental fault. Earth Planet. Sci. Lett. 477, 84–96.

Sergeev, S.A., Meier, M., Steiger, R.H., 1995. Improving the resolution of single-grain U/Pb dating by use of zircon extracted from feldspar: Application to the Variscan magmatic cycle in the Central Alps. Earth Planet. Sci. Lett. 134 (1–2), 37–51.

Shapiro, S.A., Huenges, E., Borm, G., 1997. Estimating the crust permeability from fluid-injection-induced seismic emission at the KTB site. Geophys. J. Int. 131 (2), F15–F18.

Sibson, R., 1977. Fault rocks and fault mechanisms. J. Geol. Soc. Lond. 133, 191–213. https://doi.org/10.1144/gsjgs.133.3.0191.

Tembe, S., Lockner, D.A., Wong, T.F., 2010. Effect of clay content and mineralogy on frictional sliding behaviour of simulated gouges: Binary and ternary mixtures of quartz, illite, and montmorillonite. J. Geophys. Res. Solid Earth 115 (B3).

Volpe, G., Pozzi, G., Carminati, E., Barchi, M.R., Scuderi, M.M., Tinti, E., Aldega, L., Marone, C., Collettini, C., 2022a. Frictional controls on the seismogenic zone: Insights from the Apenninic basement, Central Italy. Earth Planet. Sci. Lett. 583, 117444.

Volpe, G., Pozzi, G., Collettini, C., 2022b. YBPR or SCC′? Suggestion for the nomenclature of experimental brittle fault fabric in phyllosilicate-granular mixtures. J. Struct. Geol. 165, 104743.

Wang, L., Kwiatek, G., Rybacki, E., Bonnelye, A., Bohnhoff, M., Dresen, G., 2020. Laboratory study on fluid-induced fault slip behavior: the role of fluid pressurization rate. Geophys. Res. Lett. 47 (6) e2019GL086627.